Long-Distance Radiation of Rossby Waves from the Equatorial Current System

J. THOMAS FARRAR,[a] THEODORE DURLAND,[b] STEVEN R. JAYNE,[a] AND JAMES F. PRICE[a]

[a] *Woods Hole Oceanographic Institution, Woods Hole, Massachusetts*
[b] *College of Earth, Ocean and Atmospheric Sciences, Oregon State University, Corvallis, Oregon*

(Manuscript received 12 March 2020, in final form 9 February 2021)

ABSTRACT: Measurements from satellite altimetry are used to show that sea surface height (SSH) variability throughout much of the North Pacific Ocean is coherent with the SSH signal of the tropical instability waves (TIWs) that result from instabilities of the equatorial currents. This variability has regular phase patterns consistent with freely propagating barotropic Rossby waves radiating energy away from the unstable equatorial currents, and the waves clearly propagate from the equatorial region to at least 30°N. The pattern of SSH variance at TIW frequencies exhibits remarkable patchiness on scales of hundreds of kilometers, which we interpret as being due to the combined effects of wave reflection, refraction, and interference. North of 40°N, more than 6000 km from the unstable equatorial currents, the SSH field remains coherent with the near-equatorial SSH variability, but it is not as clear whether the variability at the higher latitudes is a simple result of barotropic wave radiation from the tropical instability waves. Even more distant regions, as far north as the Aleutian Islands off of Alaska and the Kamchatka Peninsula of eastern Russia, have SSH variability that is significantly coherent with the near-equatorial instabilities. The variability is not well represented in the widely used gridded SSH data product commonly referred to as the AVISO or DUACS product, and this appears to be a result of spatial variations in the filtering properties of the objective mapping scheme.

KEYWORDS: Pacific Ocean; Barotropic flows; Instability; Planetary waves; Rossby waves; Topographic effects

1. Introduction

There is ample evidence that Rossby waves radiate away from the major unstable current systems to affect variability at distances of up to 1000 km, but the spatial extent of this influence, and the factors determining that extent, have been difficult to assess (e.g., Bower and Hogg 1992; Miller et al. 2007). The reason for this difficulty is essentially that the observational evidence is mostly based on statistical inferences and data records that are limited in space and time, making it difficult to directly observe the wave propagation. For example, statistics of floats and moored current meter data (velocity variances and covariances) have been interpreted as evidence that deep (~1000 m) eddy kinetic energy at distances of several hundred kilometers from unstable currents such as the Gulf Stream can be explained by barotropic Rossby waves radiating from the unstable, meandering currents (Hogg 1988; Bower and Hogg 1992; Spall 1992; Waterman et al. 2011). The results have not been completely unambiguous, as the statistics show marked variability on short spatial scales, possibly a result of complex effects of topographic refraction (Bower and Hogg, 1992). Nonetheless, radiation of Rossby waves from the unstable Gulf Stream and Kuroshio extensions is believed to be responsible for the recirculation gyres that exist to the north and south of the regions where the jets flow eastward into the open ocean (e.g., Jayne et al. 1996; Mizuta 2009; Waterman and Jayne 2011; Waterman et al. 2011). Realistic general circulation model simulations show clear signs of 20–50-day barotropic waves emanating from the Gulf Stream, even at distances of 1000 km or more, but topographic effects complicate the wave properties considerably (Miller et al. 2007). Waves radiated from unstable currents are of interest because they can transmit energy and momentum efficiently over long distances and then transfer it to other motions (like the mean flow).

Farrar (2011) presented an easily visualized example of radiating instabilities in the satellite altimetry record. Tropical instability waves (TIWs) in the Pacific Ocean, which form in the east-central equatorial Pacific as a result of instability of the swift equatorial current system, are accompanied by coherent sea level variations that extend into the subtropics with the wave crests aligned in the northwest–southeast direction (Fig. 1, reproduced from Farrar 2011; Holmes and Thomas 2016). These waves have phase propagation and dispersion consistent with an interpretation as barotropic Rossby waves (Farrar 2011). Figure 1 illustrates the phenomenon with a ''snapshot'' of the SSH field after bandpass filtering to pass westward-propagating variability having wavelengths of 10°–25° of longitude and periods of 29–37 days. Although the main TIW SSH signal exceeds 10 cm near 5°N, the color scale is saturated at ±1.5 cm to emphasize the radiating variability. The color-saturated, wavelike signal seen on 10°S–10°N in the eastern-central Pacific is the SSH expression of the baroclinic TIWs; the wavelength, period, and cross-equatorial SSH structure of these unstable modes bears a close resemblance to the predictions of a linear stability analysis of the equatorial current system (Farrar 2008, 2011).

The wavelike signal seen north of the equatorial waveguide (near 10°–20°N, 110°–150°W) is phase locked to and coherent with the main TIW signal, and the space and time scales of this motion obey the dispersion relation of barotropic Rossby

Denotes content that is immediately available upon publication as open access.

Corresponding author: J. Thomas Farrar, jfarrar@whoi.edu

DOI: 10.1175/JPO-D-20-0048.1

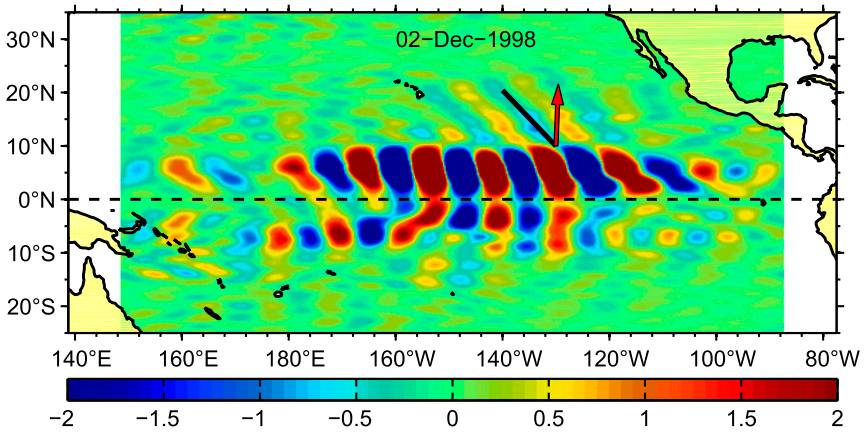

FIG. 1. Filtered SSH fields on 2 Dec 1998, after filtering to pass westward-propagating variability having wavelengths of 10°–25° of longitude and periods of 29–37 days, with the thick black line indicating the orientation of wave crests expected from the barotropic Rossby wave dispersion relation and the red arrow indicating the expected direction of group velocity. The crest orientation and group velocity direction were computed for an 11.5° zonal wavelength and a 31.5-day period. The barotropic Rossby wave dispersion relation seems to do a good job in predicting the orientation of wave crests on 10°–20°N, 120°–150°W. The figure is modified from Fig. 7a of Farrar (2011).

waves over a broad range of wavenumber–frequency space. By substituting the zonal wavenumber and frequency of the main TIW signal into the barotropic Rossby wave dispersion relation, one can make a prediction for the meridional wavenumber and the expected orientation of wave crests in latitude and longitude (Farrar 2011); this prediction agrees well with the observed orientation of the wave crests (black line in Fig. 1). Because the properties of this off-equatorial wave seem well described by the dispersion relation of barotropic Rossby waves, it seems reasonable to use that dispersion relation to estimate the group velocity; the estimated group velocity is nearly due northward at about 50 cm s^{-1} (red arrow in Fig. 1). Similar variability, also consistent with an interpretation as barotropic Rossby waves, has been seen in modeling studies (Cox 1980; Song and Zlotnicki 2004; Holmes and Thomas 2016). In a simulation of tropical instability waves in the Pacific, Holmes and Thomas (2016) inferred that a substantial fraction (>10% or about 3 GW) of the total energy lost by the equatorial current system to instability was carried away horizontally by these barotropic Rossby waves.

In the filtered SSH fields examined by Farrar (2011), the waves mostly disappear by the time they reach 20°N. Perplexingly, the same waves seen in the modeling study of Holmes and Thomas (2016) do not weaken at all before reaching 20°N. This paper seeks to address the questions: What happens to these waves? Why do they disappear? Answering these questions is an essential first step toward understanding the possible nonlocal effects of instabilities such as these on the mesoscale eddy field and the ocean general circulation, because these effects will be a consequence of how and where the waves disappear.

There are a number of plausible explanations for the apparent decay of the waves seen in Fig. 1. Farrar (2011) speculated that the decay of the waves as they reach 20°N might be a result of bottom friction. It is also possible that refraction of the waves by the topographic β effect causes the wavelength of the waves to change so much that they are no longer present within the passband of the filtered SSH field (10°–25° zonal wavelengths), or that nonlinear interactions cause the wave energy to be transferred to other wavelengths or frequencies. Another possibility is that the waves are distorted somehow in the altimetry data product used by Farrar (2011)—the DUACS[1] gridded SSH product (Pujol et al. 2016) that Farrar (2011) used is produced with a mapping algorithm that has a strong latitudinal variation in its filtering properties. (We shall see that this is the main reason why the waves seem to disappear as they travel northward).

In this paper, we adopt an analysis approach that allows us to track the waves even as their wavelength changes under refraction due to variations in the topographic and planetary β effects, and we find that SSH variability at 30-day periods is coherent with the TIW SSH signal at distances of thousands of kilometers. We produce a special-purpose gridded SSH product that has spatially uniform filtering properties, and show that spatial variations of the temporal filtering in the DUACS product (also known as the AVISO product) cause substantial attenuation and distortion of the 30-day waves in the subtropics. Using ray tracing and a barotropic numerical model, we show that the long-distance coherence observed in the SSH field can mostly be interpreted as being a result of freely propagating barotropic Rossby waves that radiate away from

[1] DUACS stands for Data Unification and Altimeter Combination System (Pujol et al. 2016), and this merged altimetry product is also often referred to as the "AVISO product." (AVISO stands for Archivage,Validation, Interprétation des données des Satellite Océanographiques).

their near-equatorial generation region. One interesting and unexpected feature of the waves is that their amplitude is extremely nonuniform in space, which we interpret as being due to the combined effects of topographic refraction, reflection, and wave interference.

The paper is organized as follows. Section 2 discusses the data and methods, including the approach used for data gridding, spectral analysis, and a preliminary ray-tracing analysis. Section 3 presents the main results of the data analysis, showing the observed long-range coherence of SSH variations with the TIW signal. Section 4 presents an interpretation of the results using a barotropic numerical model and examines how the results are distorted in the widely used DUACS gridded altimetry product.

2. Theory, data, and methods

This section discusses the rationale for the analysis methods and provides a high-level summary of how those methods were implemented. Technical details that may be of interest to some readers are given in appendices.

a. Data

The primary data used for the analysis are sea surface height anomalies from the multimission, geophysically corrected, cross-calibrated, unfiltered along-track altimetry data produced and distributed by the Copernicus Marine and Environment Monitoring Service (CMEMS; http://www.marine.copernicus.eu). (These are the same along-track data that were previously distributed by AVISO.) The data were downloaded in January 2016, and the generation of the along-track data product is described in a technical document (AVISO/CLS 2015) and in Pujol et al. (2016). We used all available altimetry data from 1992 to 2015 (AVISO/CLS 2015; Pujol et al. 2016), which includes data from the following satellite missions: TOPEX/Poseidon, *HY-2A*, *SARAL*/AltiKa, *CryoSat-2*, *Jason-2*, *Jason-1*, *GFO*, *Envisat*, *ERS-1*, and *ERS-2*.

Some of the corrections or preprocessing done to the along-track altimetry data are specifically designed to remove barotropic signals (AVISO/CLS 2015; Pujol et al. 2016), and these deserve brief discussion here. The barotropic tides are estimated from the along-track data using a data assimilating tide model (Egbert and Erofeeva 2002), and these estimates are subtracted from the along-track data (AVISO/CLS 2015; Pujol et al. 2016). Atmospherically forced barotropic signals are estimated by forcing a global barotropic model with 6-hourly pressure and wind fields from the ECMWF operational model (Carrère and Lyard 2003; Carrère et al. 2016; AVISO/CLS 2015). These barotropic signals are high-pass filtered with a 20-day cutoff (Carrère et al. 2016) and are combined with an estimate of the inverted barometer SSH signal at periods longer than 20 days to form the "dynamic atmospheric correction" that is subtracted from the along-track data. While it is possible that errors in these corrections could create confusing signals in the altimetry data made up of a combination of incompletely removed real barotropic signals and spuriously introduced modeled signals, we do not believe that these corrections have much effect on our results because 1) our analysis focuses on somewhat lower frequencies (33-day periods) and 2) our analysis focuses on SSH signals that are coherent with the tropical instability wave SSH signals.

The along-track data we used also include the so-called "long-wavelength error" (LWE) correction (appendix B; AVISO/CLS 2015) that is intended primarily to remove residual orbit errors that are correlated along the satellite track but not between adjacent tracks (Le Traon et al. 1998). This empirical correction may distort the barotropic wave signals of interest to the extent that they align with the satellite tracks and are uncorrelated between satellite passes, but we are less concerned about this possibility than the contamination by residual orbit errors.

b. Gridding of along-track data

We used the along-track altimetry data to produce a gridded SSH product intended to have temporal filtering properties that are roughly uniform in space. (The irregular time–space sampling by the various satellite altimeters makes it impossible to have truly uniform filtering properties in time or space; e.g., Wunsch 1989; Chelton and Schlax 1994; Schlax et al. 2001.) We mapped the data to a uniform space–time grid ($0.5° \times 0.5° \times 3$ days) using a Gaussian weighted-average smoother having nominal half-power points of $6° \times 6° \times 17$ days. More details are given in appendix A. For subsequent analysis, we further smoothed the gridded SSH field with a Gaussian filter having a half-amplitude wavelength of 2° in latitude and longitude. We used the gridded data from 1 January 1993 to 18 April 2015. The total record length used for analysis was 8142 days (>22 years).

There is a readily available and widely used gridded altimetry product known as the AVISO or DUACS product (AVISO/CLS 2015; Pujol et al. 2016). We initially conducted our analysis with that product, but after trying and failing to make a sensible physical interpretation of the results, we arrived at the conclusion that the spatial variations of 30-day variability in that product must be strongly affected by spatial variations in the mapping parameters (appendix B).

c. Theoretical background: Ray tracing and idealization as freely propagating barotropic Rossby waves

We would like to understand the fate of the 33-day barotropic Rossby waves seen radiating away from the equatorial currents. We will use cross-spectral analysis to isolate the part of the 33-day SSH variability that is coherent with the tropical instability wave signal, and we will attempt to interpret it as barotropic, topographic Rossby waves[2] (e.g., Rhines 1970) that propagate away from their generation region without systematic influence from subsequent atmospheric forcing. Recent work shows that realistic vertical shear of mean currents, even a surface current of only a few centimeters per second,

[2] The idealization of these waves as depth-independent barotropic waves seems like a good starting point, but it may be inadequate for a number of reasons. As is well known, the combination of stratification and topography can modify both the dispersion relation and the vertical structure of Rossby waves.

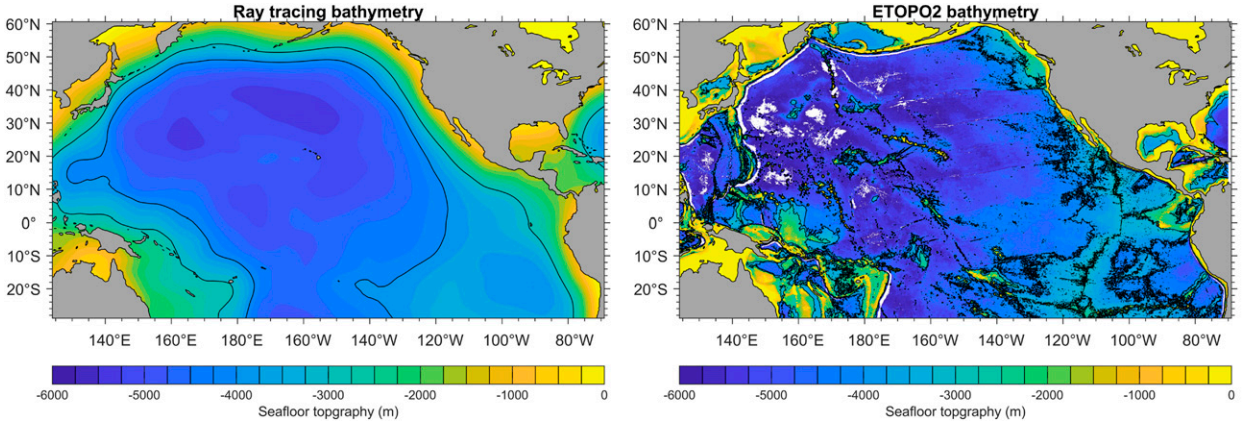

FIG. 2. (left) Smoothed bottom topography used for the ray-tracing calculation. (right) Unsmoothed bottom topography from ETOPO 2. In both panels, the 3000- and 4000-m isobaths are represented by black contours.

can appreciably affect the vertical structure of the barotropic mode (Brink and Pedlosky 2020), but this effect should be small for the wavelengths that we consider here. Throughout this paper, our use of "barotropic" is not meant to imply strict depth independence, but rather is a shorthand for a lowest-vertical-mode signal that most closely resembles the idealized barotropic mode. The phase speed and group velocity inferred by Farrar (2011) ($\sim$0.5 m s^{-1}) are large relative to the inferred particle velocities and the general current speeds of the North Pacific. A linear interpretation of the waves is thus appropriate. While subsequent atmospheric wind and pressure fluctuations will necessarily affect the waves as they travel far from their generation region, we do not expect these effects to be systematic. Assuming that the waves are not affected by the time-dependent oceanic motions, their frequency can be expected to remain constant, and a coherence analysis at the dominant TIW frequency should identify the SSH signal of the propagating waves.

Ray tracing is often the first approach used for understanding wave propagation away from a generation region. The technique assumes that changes in the propagation medium are "gradual" (i.e., on length scales much longer than a wavelength). The bathymetry of the North Pacific has many important features that do not meet this condition, such as isolated seamounts, the series of fracture zones in the eastern part of the basin, and the steep slopes south of the Alaskan Peninsula and the Aleutian Islands (Fig. 2). Nonetheless we will briefly examine a ray-tracing solution for hints of how the large-scale bathymetric features might influence the Rossby wave propagation.

We solved the ray-tracing equations in spherical coordinates following Longuet-Higgins (1965). We used topography from ETOPO 2 (version 2) smoothed with a two dimensional Gaussian smoother that has a half-amplitude wavelength of 33° (Fig. 2). The wave rays were initialized along 10°N with a frequency of 33.5 days and a zonal wavelength of $\lambda_x = 16°$ of longitude. The zonal wavenumber is negative so that the waves propagate westward. These values were chosen to be consistent with the values diagnosed in section 3. (They differ slightly from the values reported in Fig. 1, because Fig. 1 shows a snapshot in time, and the dominant TIW frequency and zonal wavelength vary from year to year, and even within a single year.) The initial meridional wavelength depends (through the dispersion relation) on the local topography but is roughly $\lambda_y = 12°$ of latitude, with a negative meridional wavenumber for poleward energy propagation away from the TIWs. The net wavelength is about 10°, consistent with the observations of Farrar (2011). With the above smoothing and initial wavenumber, the short Rossby wave dispersion relation is appropriate (Durland and Farrar 2020):

$$\sigma = \frac{\hat{\mathbf{e}}_z \cdot (\boldsymbol{\beta} \times \mathbf{K})}{|\mathbf{K}|^2}. \tag{1}$$

The positive radian frequency is σ, $\hat{\mathbf{e}}_z$ is the unit vertical vector, and $\mathbf{K}$ is the wavenumber vector. The $\boldsymbol{\beta}$ vector is defined as

$$\boldsymbol{\beta} \equiv H\nabla(f/H), \tag{2}$$

where f is the Coriolis parameter, $H(\lambda, \theta)$ is the water depth, and λ and θ are the longitude and latitude. The β vector plays the same dynamical role as ∇f in a flat-bottom solution. As the ray equations were integrated forward in time, we monitored the evolving wavenumbers to ensure the continued validity of the short Rossby wave approximation.

Figure 3 displays the ray solutions. The magenta vector pointing northwestward from 10°N, 130°W in Fig. 3 shows the initial group velocity (parallel to the ray trajectories at 10°N). The red vector shows the direction of phase propagation. The regular phase patterns and parallel ray trajectories south of 20°N are consistent with the observations of Farrar (2011). North of 20°N, the large-scale bathymetry begins to refract the rays toward a more westward direction, causing a convergence of rays in the midlatitudes between 130° and 150°W. Because the ray tracing is only a preliminary investigation, we do not calculate energy density, or treat the solutions near the caustics. The densely packed ray paths northwest of the strong convergence near 43°N, 150°W are therefore not dependable. The gradual westward refraction of the several rays closest to

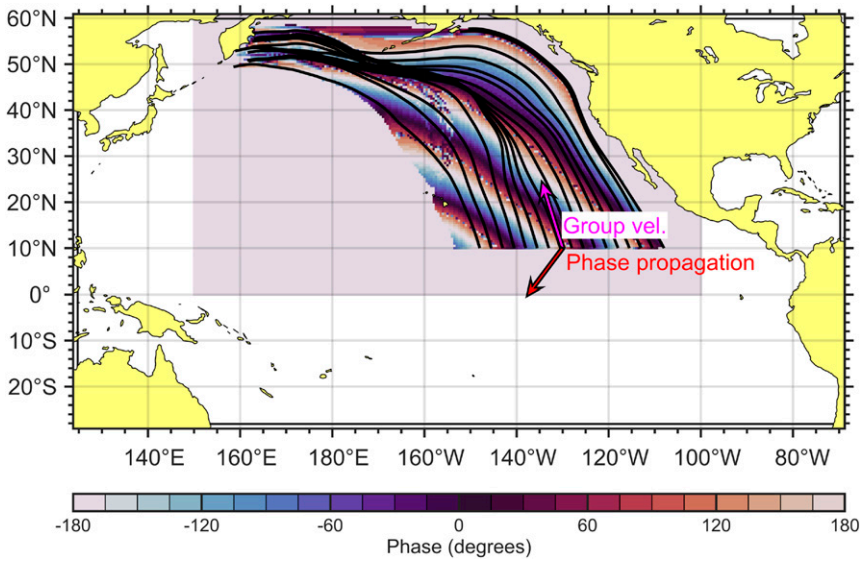

FIG. 3. Ray paths for a wave leaving 10°N with 33.5-day period and 16° zonal wavelength. ETOPO2 North Pacific bathymetry has been smoothed with a two-dimensional Gaussian smoother having a half-amplitude wavelength of 28°. Black lines indicate the paths of energy propagation, as the waves are refracted by variations in the ocean depth and the Coriolis parameter. The color shading indicates the wave phase, and the red vector shows the direction of phase propagation. The magenta arrow indicates the initial group velocity vector of the wave.

the North American continent should be viewed skeptically because the topographic smoothing has fundamentally changed the character of the wall-like bottom topography at the northern boundary, making it more like a gentle slope (Fig. 2). Nevertheless, the calculations suggest that poleward of 20°N we might expect a convergence of wave energy. They also suggest that the influence of the equatorially generated waves might be felt in the far northwestern corner of the basin.

d. Spectral analysis methods and approach

Drawing inspiration from the ray-tracing approach, we chose to carry out our data analysis in the frequency–latitude–longitude domain in order to focus on the 33-day period band without constraining the wavenumber [in contrast to the wavenumber–frequency analysis of Farrar (2011)]. We did this by estimating cross-spectral quantities, like squared coherence, gain, and phase between the SSH time series at 5°N, 130°W (where the 33-day TIW variability is strongest) and all other locations. The resulting map of squared coherence allows us to identify locations where the SSH variability is coherent with the 33-day TIW variability, the map of gain allows us to estimate the pattern of the amplitude of the coherent SSH variability, and the map of phase allows us to quantify the spatial variations of the phase of the SSH signal that is related to the TIWs. Like the ray tracing, this approach exploits our expectation that the wave frequency will be preserved as the waves propagate away from their forcing region, but, unlike the ray tracing, there is no implicit assumption that the wave propagation must change only gradually. Another difference from the ray-tracing analysis is that a broad range of zonal and meridional wavenumbers may contribute to the variability in a given frequency band—the analysis places no constraint on the wavenumber, except for the fact that short wavelengths ($<\sim 6°$) are suppressed by the mapping of the SSH data.

To estimate the frequency power spectral density ("spectrum") of SSH and the cross-spectrum of SSH between pairs of locations, we first removed the time mean of the SSH anomaly at each location and applied a taper window (a Tukey, or tapered cosine, window) that brings the time series smoothly to zero over the first and last 10% of the time series (Harris 1978). We then computed the Fourier coefficients (using MATLAB's fast Fourier transform):

$$\hat{h}(\omega) = \sum_{n=-N/2}^{N/2-1} h_n e^{-2\pi i \omega t_n}, \tag{3}$$

where h_n is the value of SSH at a given location at time n, N is the total number of data points at that location, $\omega = m/(N\Delta t)$ is the dimensional frequency (not radian), and $t_n = n\Delta t$. The frequency index m ranges over the same set of integers as the time index n does. [If N is odd, as it actually is in our analysis, the summation is over $-(N-1)/2$ to $(N-1)/2$]. In our analysis, the fundamental frequency resolution is $1/(N\Delta t) = 1/(8145 \text{ days})$.

The one-sided (i.e., positive-frequency) power spectral density (Bendat and Piersol 2010, 399–400) at each location expresses the variance of h within a given frequency band:

$$\Psi_h(\omega, \lambda, \theta) = \left\langle \frac{2\Delta t}{N} \hat{h}^* \hat{h} \right\rangle, \tag{4}$$

where the asterisk indicates the complex conjugate and the angle brackets indicate the expectation value (which we will approximate by averaging over 13 adjacent frequency bands).

The Fourier coefficient $\hat{h}(\omega, \lambda, \theta)$ expresses the amplitude and phase of SSH at the frequency ω at the longitude λ and latitude θ. If there is wave radiation from a source region that affects the SSH at the location (λ, θ) via linear wave dynamics, we would expect part of the SSH signal $\hat{h}(\omega, \lambda, \theta)$ to be linearly related to (i.e., to have a fixed amplitude and phase relationship to) the SSH in the source region. Of course, there may also be contributions to the SSH signal $\hat{h}(\omega, \lambda, \theta)$ that are completely unrelated to the SSH signal in the source region. We can express this situation as

$$\hat{h} = \alpha_h \hat{h}_0 + \hat{n}, \tag{5}$$

where $\hat{h}_0(\omega, \lambda_0, \theta_0)$ is the SSH at a reference location in the hypothesized source region, the "transfer function" $\alpha_h(\omega, \lambda, \theta)$ is a complex number that relates the amplitude and phase of the SSH at the reference location to that at the position (λ, θ), and $\hat{n}(\omega, \lambda, \theta)$ is the part of the SSH signal that is not related to $\hat{h}_0$ (i.e., that is linearly independent of $\hat{h}_0$).

We can solve for the transfer function α_h by first multiplying both sides of Eq. (5) by $\hat{h}_0^*$ and then taking the expectation value:

$$\langle \hat{h}_0^* \hat{h} \rangle = \alpha_h \langle \hat{h}_0^2 \rangle + \langle \hat{h}_0^* \hat{n} \rangle, \tag{6}$$

where we are using the shorthand notation $\hat{h}_0^2 = \hat{h}_0^* \hat{h}_0$. We have defined $\hat{n}$ as being independent of $\hat{h}_0$, so $\langle \hat{h}_0^* \hat{n} \rangle = 0$. Thus,

$$\alpha_h = \frac{\langle \hat{h}_0^* \hat{h} \rangle}{\langle \hat{h}_0^2 \rangle}. \tag{7}$$

The transfer function, $\alpha_h(\omega, x, y)$, is complex, and it is useful to write it as a magnitude and phase:

$$\alpha_h = |\alpha_h| e^{i\phi}. \tag{8}$$

The magnitude of the transfer function $|\alpha_h|$ is referred to as the "gain," and its phase φ expresses the phase shift between h and h_0 at the frequency ω. The phase of the transfer function is identical to the phase of the cross spectrum of h and h_0, so we will refer to φ as the cross-spectral phase.

We can determine the portion of the variance of the SSH at the location (λ, θ) and frequency ω that is linearly related to the SSH at the reference location by squaring Eq. (5), taking the expectation value and again using the fact that $\langle \hat{h}_0^* \hat{n} \rangle = 0$, to obtain,

$$\langle \hat{h}^2 \rangle = \alpha_h^2 \langle \hat{h}_0^2 \rangle + \langle \hat{n}^2 \rangle. \tag{9}$$

Multiplying both sides by the spectral normalization constant $2\Delta t/N$ allows us to write this in terms of the total variance of each term within the frequency band (i.e., in terms of spectral density):

$$\Psi_h = \alpha_h^2 \Psi_{h_0} + \Psi_n. \tag{10}$$

The quantity $\alpha_h^2 \Psi_{h_0}$ is the portion of the variance of the SSH at the location (λ, θ) and frequency ω that is linearly related to the SSH signal at the reference location. Dividing that quantity by Ψ_h, the total variance of SSH in the frequency band at that location, gives the fraction of the variance of h that is linearly related to the signal $\hat{h}_0$,

$$\gamma_h^2 = \frac{\alpha_h^2 \Psi_{h_0}}{\Psi_h} = \frac{\langle \hat{h}_0^* \hat{h} \rangle^2}{\langle \hat{h}^2 \rangle \langle \hat{h}_0^2 \rangle}, \tag{11}$$

which is also known as the squared coherence amplitude.

We estimated the gain and phase [Eq. (8)] and the coherence squared [Eq. (11)] between each point and the reference location (5.125°N, 130.0°W, which we will refer to hereinafter as 5°N, 130°W). We chose this reference location because it is the place where the 33-day SSH variance is strongest (section 3). We averaged over 13 adjacent frequency bands (frequencies spanning 0.0290–0.0306 cpd or periods of 32.65–34.44 days) in order to increase the number of degrees of freedom of the estimate, and we reduced the estimated number of degrees of freedom to account for the use of a taper window as described below. The center of the frequency band has a period of 33.52 days, and the frequency band is hereinafter referred to as the "33-day period band."

Application of a taper window to a time series introduces a linear dependency among adjacent Fourier frequency bands and makes frequency-band averaging less effective at increasing the number of degrees of freedom of the spectral estimate. Following Bloomfield (2000, p. 184), we accounted for the reduction of the number of degrees of freedom of the spectral analysis and coherence amplitude caused by the tapering; this approach suggests the effective number of degrees of freedom should be reduced by 10.5% relative to the number of degrees of freedom that would be expected with no tapering. We used this reduced number of degrees of freedom in the formula given by (Thompson 1979) to estimate the coherence significance level at 95% confidence. We tested the validity of this approach using Monte Carlo simulations of the coherence for random time series having red spectra and found it to be quite accurate.

Our choice of reference location for the cross-spectral calculations is not entirely arbitrary (being the site where the TIW SSH signal is strongest), but the reader may wonder whether our results are sensitive to this choice. They are not—we present some representative results using other reference locations in appendix C. We also performed an analysis similar to the cross-spectral one used here but with frequency-domain empirical orthogonal functions (e.g., Mizuta 2009), a technique that does not require use of a reference location at all—the resulting patterns of amplitude and phase were nearly identical to the ones shown here and will not be discussed. (We prefer the cross-spectral analysis because it is simpler).

3. Observed 33-day SSH variability

The SSH field in the equatorial Pacific exhibits strong variability at periods of about 33 days (e.g., Lee et al. 2018; Farrar 2008, 2011; Lyman et al. 2005). We can quantitatively assess the spatial pattern of this 33-day variability by estimating the frequency spectral density of SSH at each location and displaying a map of the spectral density in the 33-day period

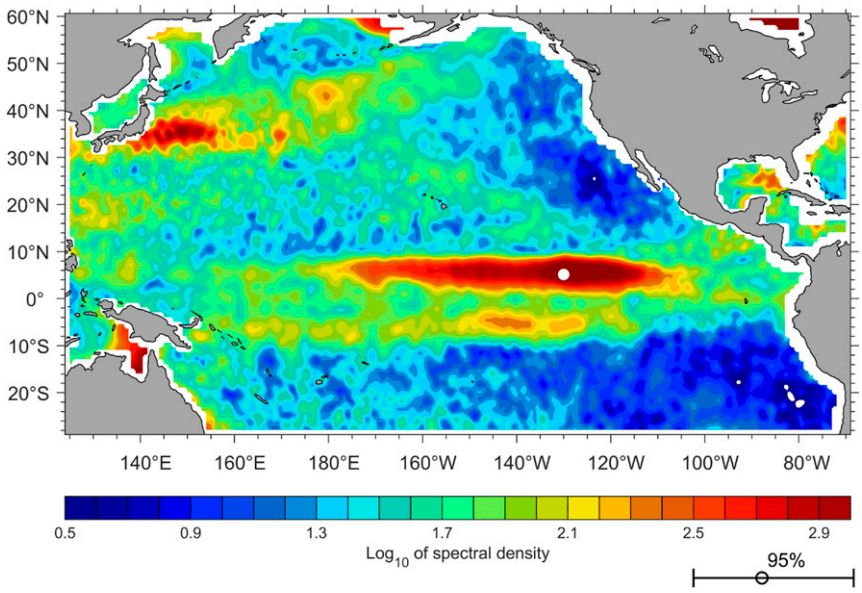

FIG. 4. Base-10 logarithm of spectral density of SSH ($cm^2\ cpd^{-1}$; proportional to variance or squared amplitude) in the 33-day period band. The 95% confidence interval for the spectrum is shown on the bottom-right side of the color bar spectral differences of about 6 contour levels can be considered statistically significant. The white circle at 5.125°N, 130°W indicates the position used for the reference time series.

band (Fig. 4). There is a broad, zonally elongated ridge of high variance near 5°N in the eastern and central Pacific (100°–170°W) associated with the 33-day TIW activity, and there is another, weaker ridge near 5°S associated with the Southern Hemisphere expression of the TIWs.

The SSH variability is strongest near 5°–6°N, 130°W (Fig. 4), and the existence of this local maximum in 33-day SSH variance is clearly due to the TIWs. We will thus use 5°N, 130°W as a ''reference location,'' and we will sometimes refer to the 33-day SSH variability at this location as the ''33-day TIW signal.'' The 33-day variability is also strong in the Kuroshio Extension region, but as we will see, this variability is not coherent with the TIWs.

A remarkable feature of the map of the spectral density in the 33-day period band (Fig. 4) is that it is extremely patchy, with order-of-magnitude changes in variance over distances on the order of 1000 km (10°) or less. This is not only true when comparing the unstable current jets (equatorial currents and Kuroshio) with the midocean gyres—it is also true when comparing the SSH variance in one open-ocean region with another. This patchiness does not appear to be a mere result of noise or lack of stability in the spectral calculation (differences in variance of 6 contour levels exceed the estimated 95% confidence interval, and this corresponds to about a factor of four in variance). For example, there is about a factor of 20 change in variance between the local minimum of variance near the Baja Peninsula (western Mexico) and the relative maximum 1500 km to the southwest near 20°, 140°W, and there is a factor of 5 change in variance between the local minimum near 10.5°N, 140°W and the location 390 km due north of there (near 14°N, 140°W)—these differences exceed the 99% confidence interval. Below, we interpret this patchiness as being a dynamical consequence of topographic refraction, reflection, and interference of the radiating waves.

We estimated the coherence between the SSH time series at 5°N, 130°W (the reference location) and the SSH at all other locations (Fig. 5). Throughout a large region of the tropical and North Pacific,[3] the 33-day SSH signal is coherent with that in the TIW region at high levels (squared coherence >0.5) that are different than zero at 95% confidence or better (indicated by a white contour in Fig. 5). Hereinafter, we will sometimes refer to the squared coherence amplitude as the ''coherence,'' and we will sometimes omit specific mention of the 33-day period band, although it should be understood that all results apply to this period band (section 2).

[3] We only display the results for the tropical and North Pacific because this is where the most robust coherence pattern is detected. Previous work looking for evidence of radiation in the tropics and the immediate vicinity of the TIWs mostly found radiation only to the north (Farrar 2011). We have checked again and could not find clear evidence of radiation farther into the South Pacific. One might imagine this could be because the TIWs are stronger on the northern side of the equator. However, realistic model simulations show clear evidence of southward radiation (e.g., Holmes and Thomas 2016), so this needs further investigation. The model simulations of Holmes and Thomas (2016) and Cox (1980) showed southward radiation but did not have realistic topography, which suggests the lack of southward radiation in the observations could be a dynamical consequence of topography. We return to this point in the discussion (also see Fig. 8).

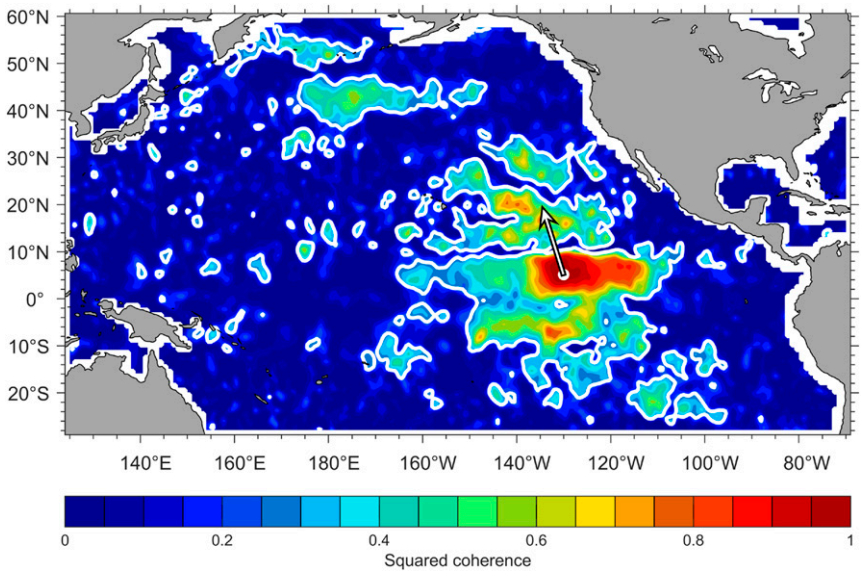

FIG. 5. Squared coherence (dimensionless, ranging from 0 to 1) between SSH in the 33–34-day period band at 5°N, 130°W (white circle) and all other locations. The squared coherence gives the fraction of variance explained at each location (at 33-day periods) by the SSH at the reference location. White contours surrounding regions of high coherence represent the level at which the coherence is different from zero at 95% confidence. The white arrow shows the expected direction of propagation of barotropic Rossby wave energy (assuming a 33-day period and 16° zonal wavelength).

There is a region of high coherence in the main TIW region (±10° from the equator), with ridges of high coherence found along 5°N and 5°S where the TIW variability is strong (Fig. 5). The SSH along 5°S is coherent with the 33-day SSH signal at 5°N, reflecting the expected mode-like structure of the TIWs (Lyman et al. 2005; Farrar 2008, 2011). The coherence between the reference location (5°N, 130°W) and its ''mirror-image'' location south of the equator (5°S, 130°W) is higher than the coherence between the reference location and locations just one TIW wavelength (about 15° of longitude) to the west.

There are also many locations outside the immediate TIW region where the SSH variability is significantly coherent with the 33-day TIW SSH signal at the reference location (Fig. 5). The spatial pattern of coherence has a patchy character (for which we will later offer a physical interpretation). There are fairly large patches of significant coherence as far south as 20°S and as far north as 50°N, adjacent to the Aleutian Islands off Alaska and the Kamchatka Peninsula in Russia (northeast of Japan). There are also many smaller patches of statistically significant coherence, with radii of a few degrees or less, scattered throughout the Pacific Ocean (and even the Atlantic Ocean)—we should not overinterpret these fine details of the coherence map, because we expect the 95% significance level to be exceeded at 5% of the locations as a result of pure chance.

Outside the immediate TIW region (~10°N–10°S), there are several large patches exhibiting significant coherence with the TIW SSH signal. The largest of them spans the 10°–20°N region and is the same region studied previously by Farrar (2011). Squared coherence amplitudes exceed 0.6 over much of this region, indicating that more than 60% of the variance of SSH at 33-day periods can be predicted from the TIW signal at the reference location. There is another large patch just to the north, near 30°N, 125°–140°W, and there are two more large patches of significant coherence to the northwest near 40°–50°N. In all of these patches, the squared coherence amplitude is roughly 0.5 or higher, indicating that half of the SSH variance at 33-day periods can be predicted from the TIW signal.[4]

It is remarkable that the squared coherence amplitude is higher in many of these distant patches than it is only 15°–20° to the east or west or the reference location. This is somewhat surprising because the TIW propagation is due westward, and so one would expect the coherence to be highest to the west or east of the reference location. One possible reason for the low coherence at locations to the east and west in the TIW region is that the TIW variability contains different wavenumbers at the same frequency (Farrar 2011), which would be expected to degrade the coherence.

The associated map of phase (Fig. 6) shows the expected patterns of (i) the baroclinic TIWs in the equatorial waveguide

[4] The reader may wonder whether the spatial patterns of the squared coherence amplitude, and associated spectral quantities like gain and phase, are sensitive to the choice of reference location. We have examined this sensitivity, choosing reference locations inside and outside the other patches of high coherence. The detailed patterns of coherence, gain, and phase do depend on the choice of reference location, but in a way that is consistent with the hypothesis that barotropic wave propagation is responsible for the observed long-range coherence (appendix C).

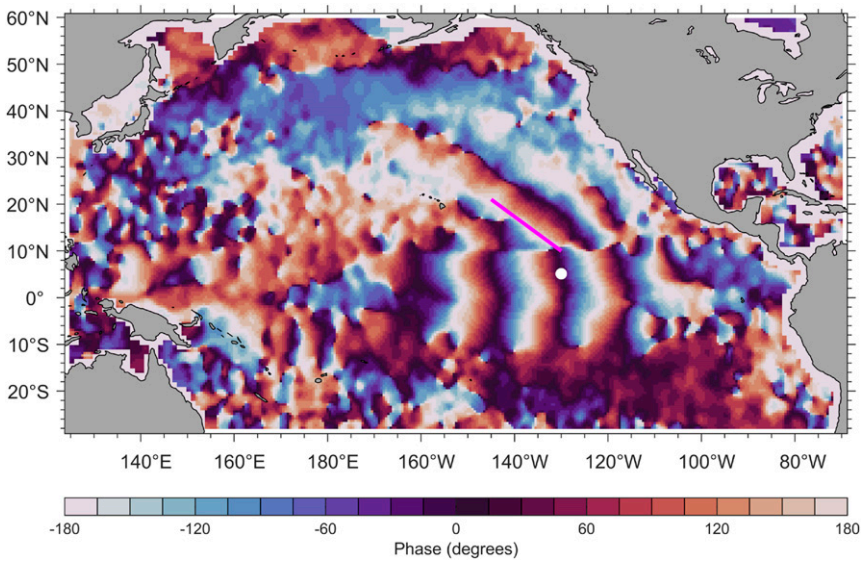

FIG. 6. Coherence phase (°) between SSH in the 33–34-day period band at 5°N, 130°W (black circle) and all other locations. The sign convention of phase is such that phase at a fixed geographical position progresses in time from blue to white to red (i.e., from positive values to negative values). The magenta line shows the expected orientation of barotropic Rossby wave crests at 33.5-day periods and the zonal wavelength of the TIWs (estimated to be 16° of longitude).

(~10°N–10°S) with dominantly westward phase propagation and (ii) the northwest-to-southeast oriented phase lines associated with northward-radiating barotropic Rossby waves in the region immediately north of the strongest TIW activity (i.e., 10°–20°N, 115°–155°W). As in the ray tracing, these phase lines extend northwestward in fairly straight lines to as far as 35°N, where they begin to bend toward a more westward direction. Farther poleward, the phase isolines take a more east–west orientation, with a large region of in-phase behavior (i.e., more gradual phase variations) in the northeast Pacific near 45°N and 175°E–145°W. The reader might notice that the zonal wavelength in the 10°–20°N region is somewhat longer in Fig. 6 than it is in Fig. 1—Fig. 6 is a composite over the whole record, whereas Fig. 1 represents a particular time, and there is some year-to-year variability in the dominant wavelength and frequency of the TIWs and the radiated variability.

We can obtain an estimate of the relative amplitude of variability coherent with the TIW SSH signal by estimating the gain relative to the SSH at the reference location. The resulting map of the gain in the 33-day period band (Fig. 7) has a pattern that is similar to the map of coherence, with elevated gain in the TIW region, in the 10°–20°N region to the north of the TIW region, and in a region spreading to the northwest around 40°N. To get a measure of which parts of the gain estimate are most robust, we estimated the relative error of the gain following Bendat and Piersol (2010, p. 309, their Eq. 9.90), and we included a white contour in Fig. 7 to indicate the places where the gain error is estimated to be less than 30% of the estimated gain. The pattern of the relative error in the gain closely resembles the pattern of coherence amplitude. There are small patches of high gain in the Kuroshio extension region (around 35°N near Japan) that are of questionable significance—the estimated coherence in this region was insignificant, the relative error in the gain was above 30%, and we suspect the high gain values are the spurious result of high variance coupled with the inevitable bias of coherence estimates near zero.

4. Interpretation and discussion

There were two important results in the previous section. 1) There is SSH variability at distant locations throughout the North Pacific that is coherent with the SSH signal of tropical instability waves. At locations 3000 or even 6000 km away from the unstable equatorial currents, about half of the SSH variance at 33-day periods can be explained by the TIW SSH signal. 2) These remote, coherent signals exhibit remarkable "patchiness" in their spatial patterns, with substantial amplitude variations over hundreds of kilometers. This patchiness is reflected in the pattern of variance (spectral density) and the coherence amplitude and gain relative to the place where the TIW signal is largest.

It is clear from prior work that barotropic Rossby waves radiate energy northward from the unstable equatorial currents, which provides a seemingly obvious interpretation of the coherence of remote SSH variability with the TIW SSH signal. However, the patchiness of the coherence, with regions of high coherence separated by regions of low coherence, might cause one to question this interpretation. Below, we make some general comments on the likely influence of bottom topography, and then use a simple barotropic model with realistic topography to examine the question of whether the observed pattern of coherent SSH variability is consistent with the

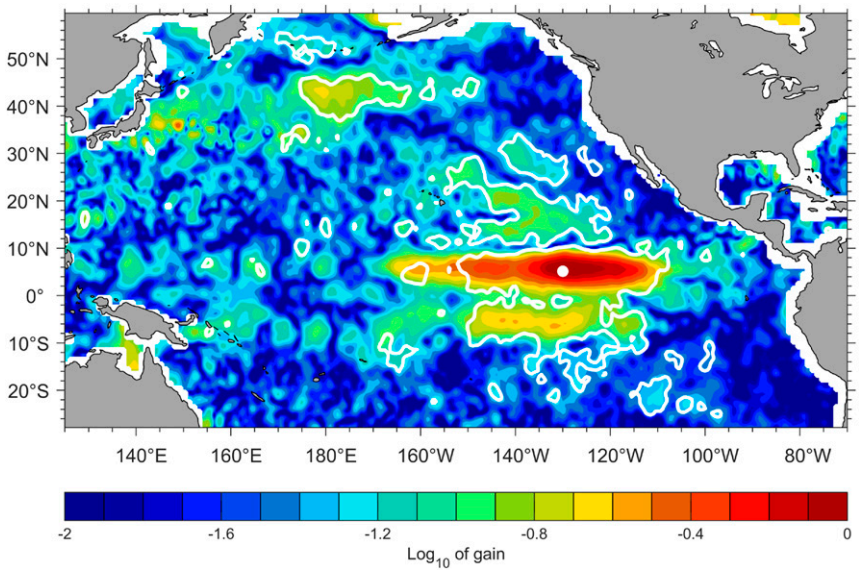

FIG. 7. Base-10 logarithm of gain factor between SSH in the 33–34 day period band at 5°N, 130°W (white circle) and all other locations. Inside the white contours, the relative error in the estimated gain is estimated to be less than 30%. For reference, note that at locations where the base-10 logarithm of the gain is −0.8 the amplitude of 33-day SSH variability is about 16% (or $10^{-0.8}$) of the maximum TIW SSH signal.

barotropic Rossby wave interpretation. We conclude the paper by revisiting the question of why the waves seemed to disappear in the analysis of Farrar (2011).

a. *Effects of topography on the SSH pattern of the radiated waves*

The position and slope of major features of the seafloor are expected to exert an important influence on the behavior of barotropic Rossby waves. The preliminary ray-tracing analysis (section 2c) was intended to account for the effect of the sloping seafloor on the wave propagation. It may have yielded some useful insights, at least insofar as it helped guide our data analysis by giving an idea of what could happen, but there are important ways that the seafloor topography varies on length scales shorter than a wavelength (nominally 1000 km). Perhaps most important, the transition from the abyssal plain (>4000-m depth) to the continental shelf (~200-m depth) occurs over less than a wavelength along much of North America, and there are many other abrupt changes in ocean depth. The topographic smoothing needed for the application of the ray tracing suppresses two of the main ways that topography could contribute to small-scale variations the wave amplitude: via small-scale refractive effects and via reflections from steep bathymetry.

Inspection of the pattern of the SSH coherence together with the topographic contours (Fig. 8) reinforces the idea that abrupt changes in bottom topography may be an important factor affecting the pattern of the wave amplitude. The regions where there is high coherence with the TIW SSH signal lie almost exclusively on or adjacent to the abyssal plain, and the wave signal seems to be largely bounded by the regions of steep topography. The steep topographic features visible in Fig. 8 are completely missing from the ray-tracing analysis (Fig. 2).

To get some further insights into the question of whether the observed pattern of coherent SSH variability could result from the radiated waves propagating over realistic topography, we conducted some idealized numerical experiments with a barotropic ocean model. The numerical model solves the linearized, barotropic, primitive equations on a sphere, and we ran the model with 1) a flat-bottom ocean with no continents, 2) a flat-bottom ocean with continents, and 3) realistic topography. We are conducting an ongoing analysis of the model behavior (Durland and Farrar 2021, unpublished manuscript), and we present some preliminary results here.

The most important model details are as follows, and more details are in appendix D. The model domain covers only the North Pacific, and the model is forced at its southern boundary by an oscillating pressure signal with a period of 33.5 days and a specified zonal distribution of amplitude and phase propagation. The southern boundary is at 9.5°N, where the observed phase patterns make the transition from TIW-like phase to barotropic Rossby wave-like phase (see Fig. 6). The intent is to force a reasonably realistic wave field at 9.5°N and see how it propagates. The forcing is nonzero only between 170° and 100°W, the region where the TIW amplitude is strongest (e.g., Fig. 7). The model is spun up from rest, with the forcing increased gradually from zero to full strength over about 3 weeks. Integration is continued until the model reaches a stationary oscillatory state, typically within about 3 periods (100 days). After the model converges, we estimate the model SSH amplitude and phase by fitting a 33.5-day sinusoid to the model SSH.

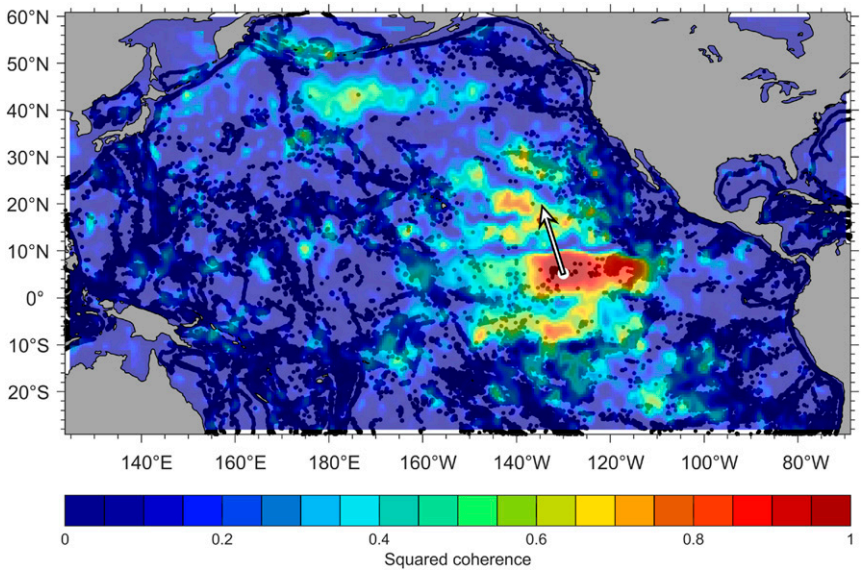

FIG. 8. Squared coherence between SSH in the 33–34-day period band at 5°N, 130°W (white circle) and all other locations (colors, same as Fig. 5). Black contours indicate the 2000-, 3000-, and 4000-m isobaths. The white arrow shows the expected direction of propagation of barotropic Rossby wave energy (assuming a 33-day period and 16° zonal wavelength). The coherence has been overplotted on the bathymetric contours with some transparency in an effort to make it possible to see both fields at once.

For the model run with realistic topography, the amplitude and phase of the boundary forcing were set to the observed coherence gain and coherence phase at the latitude of our southern boundary, which is our best approximation of the actual barotropic wave field at this latitude. Given the uncertainty in the estimated gain and the likelihood that both barotropic and baroclinic motions make some contribution to the SSH signal that goes into the gain estimate at 9.5°N, we expect discrepancies between the observations and the model output.

Nevertheless, the qualitative agreement between the modeled and observed SSH patterns is reasonably good between 10° and 35°N (Fig. 9). The general envelope of elevated SSH variability sweeps to the northwest from the generation region in both the model and the observations (in agreement with the ray-tracing results). The model SSH exhibits patchiness on the same spatial scales as in the observations (a few hundred kilometers), and many of the local maxima occur in roughly the same regions in the model and the observations. (This can be seen by comparing the reference letters in Fig. 9, which are in the same location in each panel).

In both the model output and the observations, the elevated amplitudes between 20° and 35°N are roughly aligned in a ridge–trough–ridge pattern (spanning points A–E) that parallels the overall envelope (ridges running southeast to northwest), with ridges separated by roughly the wavelength of the directly forced short Rossby waves (Fig. 9). Gain in the model and observations is higher along a line between letters E and G, and again along a line passing through C and F, with a trough between these lines passing through D. We have run the model with a wide variety of forcing patterns, and a subtle ridge–trough–ridge pattern invariably shows up between about 20° and 35°N. The precise locations of the ridges depend on the forcing pattern, and the ridge locations appear to influence which topographic features produce significant maxima in the SSH amplitude.

The evidence from the modeling suggests that the ridge–trough–ridge pattern is the product of interference between the directly forced short Rossby waves and long Rossby waves that are generated by reflection from the North American coast and/or partial reflection and large-scale refraction by bottom topography. The phenomenon is most easily seen in a flat bottom model with a simplified forcing structure, in which case only the coastal reflection is involved. As in the topographic model, the simplified forcing is confined to the latitude range 170°–100°W. The amplitude is a smoothed version of the TIW amplitude at 5°N, and the zonal wavelength is 16° (propagating westward).

Figure 10 shows the evolution of the variance[5] for the flat-bottom model, with and without a continental boundary

[5] The time-evolving variance is computed as the squared SSH averaged over half of a wave period (the reported time is the center of the averaging time span). When the model reaches a stationary oscillatory state, this variance is half the square of the amplitude. When the model is still evolving, the variance still provides a good measure of the instantaneous amplitude, as long as changes in amplitude over half the period are small relative to the amplitude at the center of the variance calculation (which is the case in our model evolution).

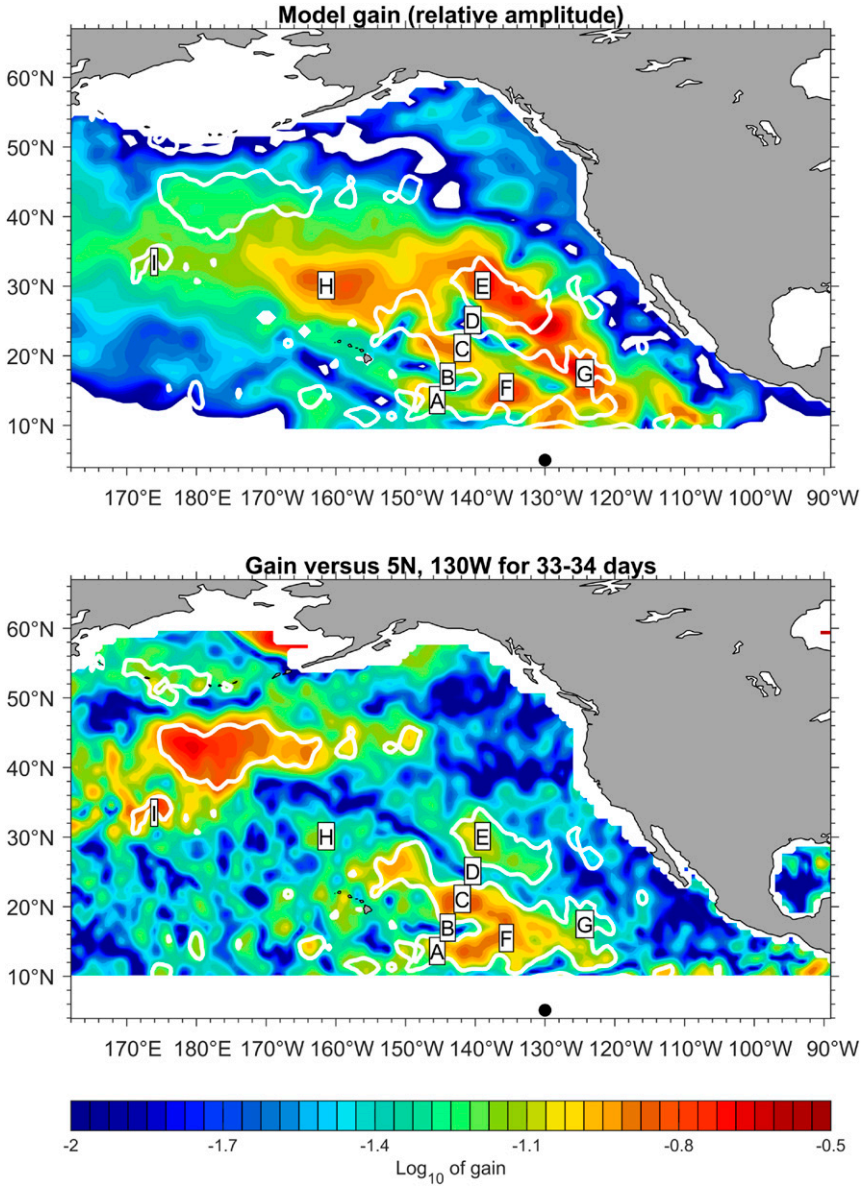

FIG. 9. (top) Log_{10} of model SSH amplitude. (bottom) Log_{10} of observed gain (or amplitude of coherent variability) relative to 5°N, 130°W (black circle). The white contours (repeated in both panels) delineate the regions where the relative error in the observed gain is estimated to be less than 30%. The letters A–I specify locations to facilitate comparison. The series of amplitude highs and lows indicated by points A–E and the horseshoe pattern connecting points A–F–C are robust features in the model and observations; in the model, these features arise from an interference pattern caused by a superposition of waves radiating directly from the TIW region and ones that reflect off the North American continental slope.

(which we are calling the ''bounded'' and ''unbounded'' model experiments). In these flat-bottom simulations, the only refractive influence on the waves is the gradient of the Coriolis parameter [Eqs. (1) and (2)] (Smith 1971; Durland and Farrar 2020). For the wavelength and frequency of interest here, we would expect the waves to leave the forcing region and refract anticyclonically under the influence of the β effect, in agreement with predictions of energy flux refraction on a sphere (Smith 1971). This can be clearly seen in the time evolution of the amplitude in the unbounded flat-bottom experiment (Fig. 10, left column). The spatial variations in the unbounded experiment are primarily on scales larger than a wavelength, although there are weak ridges separated by about half a wavelength. These are associated with the time-evolving

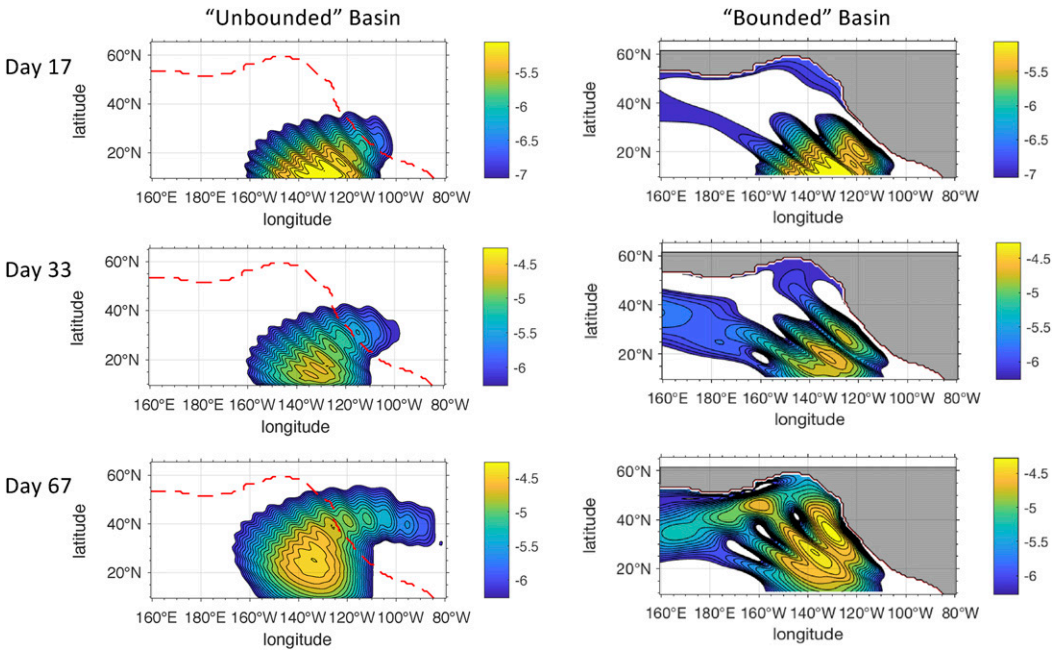

FIG. 10. Evolution of half-period SSH variance (base-10 logarithm of meters squared) in the (left) unbounded flat-bottom model and (right) bounded flat-bottom model.

amplitude, and they disappear when the model reaches a stationary oscillatory state (see bottom-left panel below about 20°N).

The evolution of the variance is much different in the flat-bottom model when there is a continental boundary (Fig. 10, right column). There are more pronounced ridges separated by about a wavelength that develop quickly, within about one period of the onset of the forcing, and do not vanish as regions approach a stationary oscillation. There is also significant variance to the north and west of the forcing region, in contrast to the unbounded model experiment. These differences are obviously a consequence of the introduction of the continental boundary in the bounded experiment.

We expect that the wave energy seen propagating northeastward in the unbounded experiment (Fig. 10, left column) would reflect if it encountered the North American coast, generating westward propagating long Rossby waves. In Fig. 11 we see that this is indeed the case. The top panel shows a snapshot of SSH in the unbounded model during the initial adjustment after the onset of the forcing (at day 16.76), and the middle column shows a snapshot of SSH in the bounded model at the same time. The bottom panel shows the difference between the two solutions: the bounded solution minus the unbounded solution (over the part of the domain where the difference is meaningful). The reflection by the North American coast generates a long-wave plume that propagates westward across the basin. The maximum amplitude of the plume is smaller than the maximum amplitude of the short waves, but in the middle latitudes, the amplitudes of the short and long waves are comparable.

To see how interference between the directly forced short waves and the long waves reflected from the North American coast can produce the ridges that we see in the variance of the bounded model (Fig. 10, right column), consider a simple one-dimensional example of two waves with the same frequency (ω): a long wave of amplitude η_1 and vanishing wavenumber superimposed on a monochromatic short wave of amplitude η_0 and wavenumber k_0. The combined signal is

$$\eta = \eta_0 \cos(k_0 x - \omega t) + \eta_1 \cos(\omega t). \tag{12}$$

The origin of the x coordinate is chosen where the waves are in phase (the amplitudes are real). The half-period variance of this superposition is

$$\overline{\eta^2} = \frac{\eta_0^2 + \eta_1^2}{2} + \eta_0 \eta_1 \cos(k_0 x). \tag{13}$$

The last term in Eq. (13) represents the interference between the wave fields, and it produces ridges in the variance that do not propagate, but which are separated by the short wavelength, as in the right panels of Fig. 10.

The variance ridges in the converged topographic model (Fig. 9, top panel) are not as pronounced as those in Fig. 10 because the long-wave generation is not as robust in the topographic model as in the flat-bottom model. In addition, the complex bathymetry, the general upward slope of the bottom between the central and the eastern North Pacific, and the various fracture zones provide numerous venues for reflection and large-scale refraction that complicate the long-wave pattern in the topographic model. Nevertheless, both the long waves and the subtle variance ridges are an underlying feature of the topographic model's response in a wide variety of forcing scenarios.

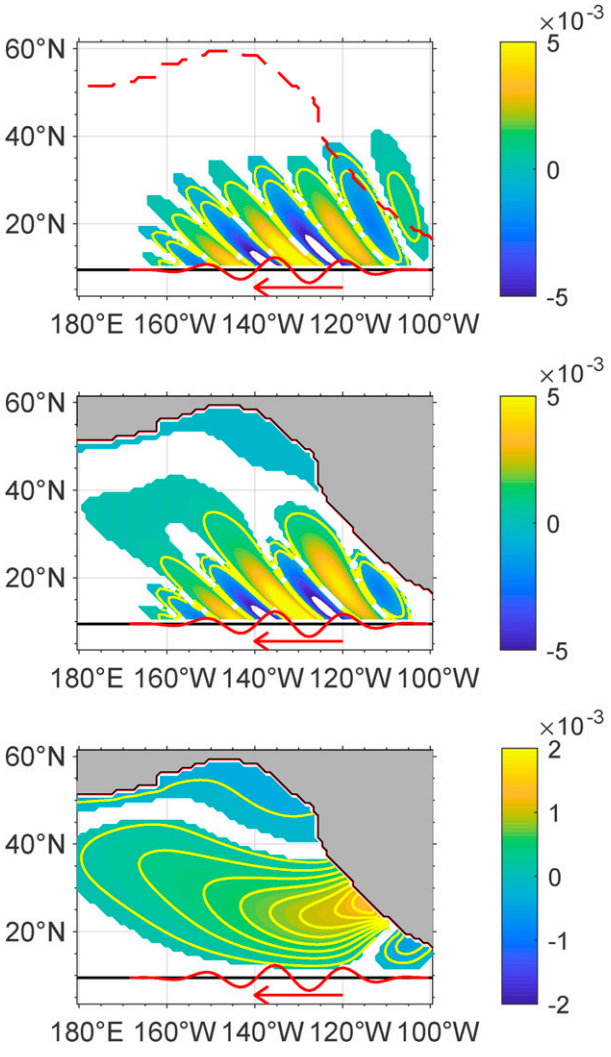

FIG. 11. Snapshots of model SSH (m) at day 16.76 after forcing onset for the bounded vs unbounded experiments in the flat-bottom model, showing the (top) unbounded model, (middle) flat-bottom model with the North American coastline, and (bottom) difference solution (bounded minus unbounded). In the top panel, the location of the coastline is shown as a dashed line for reference. The simplified forcing pattern is shown in red along the southern boundary of each panel.

The qualitative agreement between the modeled and observed amplitude patterns is reasonably good, especially south of about 35°N, but the quantitative agreement is not good, in the sense that almost none of the relative maxima and minima in the model are in precisely the same positions as the maxima and minima in the observations. This is consistent with the interpretation that the patchy pattern of SSH amplitude and coherence is partly a result of wave interference, because the interference pattern of two waves will be very sensitive to the wavelength and relative phase of the waves. Slight differences in the wavenumber content of the forcing or inaccuracies in the modeled physics of the reflection process would be expected to cause substantial shifts in the locations of constructive and destructive interference.

The small-scale patchiness in the model appears to arise from refraction and partial trapping of the incident wave field by topographic features with sharp horizontal curvature, such as seamounts and the ends of topographic ridges. The location of the variance ridges produced by the wave interference determines which topographic features actually produce noticeably elevated SSH variance, and this interplay of wave interference and topography is dependent on the structure of the model forcing. The model results do show that it is reasonable to interpret most of the observed coherent SSH variability as being due to the barotropic waves radiated from tropical instability waves, especially within about 3000 km of the instabilities. The more distant feature near 44°N, 180° is not well reproduced by the model. The SSH at this location is unquestionably coherent with the SSH signal in the TIW region—about half of the variance of SSH at 33-day periods at 44°N, 180° can be predicted from the time series of SSH in the TIW region—but because we cannot reproduce the feature in a model or clearly understand how it would be generated by the radiating waves, we cannot confidently ascribe the feature at 44°N, 180° to the radiating waves. It would be interesting to consider whether atmospheric wind and pressure forcing could force SSH signals that would be coherent with the TIW SSH signal.

b. *Conclusions*

In the introduction, we discussed the fact that the waves seemed to weaken dramatically and disappear near 20°N in the previous analysis by Farrar (2011). We posed the questions: What happens to these waves? Why do they disappear? We now have some insights into the answers to these questions.

On the question of what happens to the waves, we can conclude that the waves travel well north of 20°N. The data analysis and the modeling here both suggest that the waves travel to around 30°N with little decrease in SSH amplitude. The ultimate fate of the wave energy is not clear—the model shows the energy dissipating steadily as the waves move northward, but the observations show that the amplitude of the SSH signal coherent with the TIWs actually increases again near 45°N, 180°. The reasons for this increase in amplitude remain a mystery—it is possible that it is deep basin resonance similar to those described by Weijer et al. (2007) and Weijer (2008) that the model fails to reproduce, and it is possible that atmospheric forcing is a factor.

On the question of why the waves disappear by the time they reach 20°N, we have concluded that they do not in fact disappear. The better question is, "Why do the waves disappear near 20°N in the analysis of Farrar (2011)?" Two possible explanations mentioned in the introduction were that 1) refraction of the waves by the topographic β effect could cause the wavelength of the waves to change so much that the zonal wavelength is no longer within the passband of the filter that was used (10°–25° zonal wavelengths), and 2) that the waves might be distorted by the latitudinal variation in the filtering properties of the gridding algorithm used to produce DUACS gridded SSH product (Pujol et al. 2016). The first of those factors, alteration of the wavelength of the waves by refraction, is definitely relevant—Fig. 6 clearly shows that the zonal wavelength becomes longer as the waves move beyond 20°N.

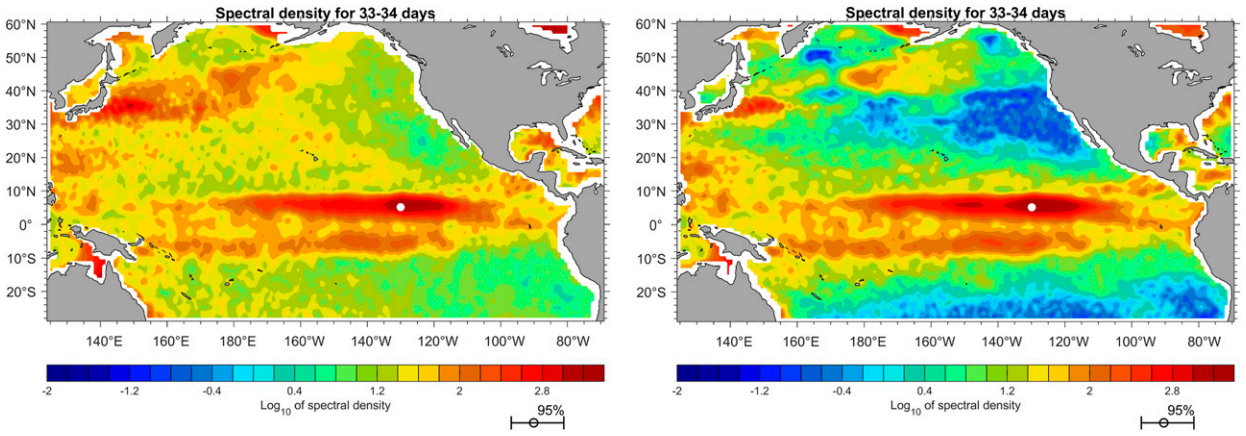

FIG. 12. (left) Base-10 logarithm of spectral density of SSH ($cm^2\ cpd^{-1}$; proportional to variance or squared amplitude) in the 33-day period band, computed from the gridded SSH product used here and described in appendix A. This plot is identical to Fig. 4, but with an expanded dynamic range in the color scale. (right) The same quantity computed using the DUACS2014 gridded SSH product (Pujol et al. 2016). In both panels, the 95% confidence interval for the spectrum is shown on the bottom-right side of the color bar. The gridded SSH product used in the left panel has spatially uniform temporal filtering, and we suspect that the difference in spatial patterns of 33-day variance is mostly due to spatial variations in temporal filtering in the DUACS product.

However, the second of those factors (spatial variation of the temporal filtering in the DUACS gridded SSH product) is apparently the dominant one. The objective analysis method used to produce the DUACS product requires specification of autocovariance functions for the variability and for the measurement errors, which together set the filtering properties of the mapping algorithm. The values used in the autocovariance function for the DUACS mapping algorithm are not publicly available, but the zonally averaged temporal correlation scales used in the autocovariance function reach a maximum in the 20°–40°N and 20°–40°S latitude bands (see Pujol et al. 2016, their Fig. 4), which suggests that, on average, this is where high-frequency variability will be most strongly suppressed.

We performed an analysis identical to the one that led to the plots of 33-day spectral density, squared coherence amplitude, phase, and gain (Figs. 4–7), except that we used the DUACS2014 product (appendix B). In the major regions of high 33-day variance (the tropical Pacific, the Kuroshio Extension, and the high-amplitude spot in the North Pacific), the two SSH products are very similar—the 33-day spectral density agrees within error bars (Fig. 12), and the patterns of coherence amplitude and phase are similar. However, at the basin scale, the spatial patterns of 33-day variance are dramatically different in the two products; in the 20°–40°N latitude band of the eastern Pacific that has been the focus here, the 33-day spectral density is lower by a factor of roughly 100 in the DUACS product (Fig. 12). The ridge of elevated SSH variance caused by the barotropic Rossby waves east of Hawaii is completely absent. The SSH maps used here and the DUACS product were constructed from the same along-track data, with the same corrections. The only difference is that the gridded SSH product used here was deliberately constructed to have spatially uniform temporal filtering, so we are led to conclude that the spatial pattern of 33-day variance in the DUACS product must be dominated by the assumed form of the autocovariance function used for the objective mapping scheme.

Acknowledgments. The along-track altimetry data used in this study are produced and distributed by the Copernicus Marine and Environment Monitoring Service (CMEMS) (http://www.marine.copernicus.eu). This work was supported by NASA Grants NNX13AE46G, NNX14AM71G, and NNX17AH54G. We are grateful for the helpful comments and criticism provided by two anonymous reviewers. We thank Dudley Chelton, Gerald Dibarboure, Joe Pedlosky, Ryan Holmes, Rick Lumpkin, Shafer Smith, Cesar Rocha, and Navid Constantinou for helpful discussions.

Data availability statement. Intermediate data products and computer code to reproduce some of the results of this study are available in repositories at https://doi.org/10.5281/zenodo.4541592 (data products) and https://doi.org/10.5281/zenodo.4549917 (code).

APPENDIX A

Gridding of Along-Track Altimetry Data

Although there is a readily available and widely used global gridded data product, often referred to as the DUACS product (Le Traon et al. 1998; Ducet et al. 2000; Le Traon et al. 2003; Pujol et al. 2016), this product has considerable spatial structure in its space/time smoothing that attenuates 30-day variability in the midlatitudes. We thus found it desirable to create a mapped product with uniform spatial and temporal smoothing. We did this using the following procedure:

1) We averaged the altimetry data along-track in 0.25° latitude bins.
2) We mapped the data to a uniform space–time grid (0.5° × 0.5° × 3 days) using a Gaussian smoother (weighted average) having nominal half-power points of 6° × 6° × 17 days. Specifically, the SSH (h_n) at each grid point was estimated

as a weighted average of the measured SSH (g_m) at the nearby points as follows:

$$h_n = \frac{\sum_{m=1}^{M} e^{-2(ar)^2} g_m}{\sum_{m=1}^{M} e^{-2(ar)^2}} \quad \text{with} \tag{A1}$$

$$r^2 = \frac{x^2}{L_x^2} + \frac{y^2}{L_y^2} + \frac{t^2}{L_t^2} \quad \text{and} \tag{A2}$$

$$L_{x,y,t} = \frac{0.775}{\omega_{\text{cutoff}}} \tag{A3}$$

where x, y, and t are the longitude, latitude, and time distances from the grid point, $a = 3$, and ω_{cutoff} is the nominal half-power frequency of the gridding kernel in a given dimension (latitude, longitude, or time). The summation is carried out using all of the M along-track measurements that are within the scaled distance $|r| < 1/2$ of the grid point being estimated. The properties of this Gaussian smoothing window and its associated filter transfer function are discussed, for example, by Harris (1978) and Schlax and Chelton (1992).

3) If the number of SSH observations within $|r| < 1/2$ of the grid point being estimated was less than 6 [i.e., $M \leq 5$ in Eq. (A1)], no estimate was made. This happens only rarely and appears to be associated with brief satellite data outages during times when there were only two operating altimeters (e.g., around December 1995). When these gaps occur, they are of limited zonal extent, and the gaps are filled by linear interpolation in longitude.

APPENDIX B

Barotropic Wave Signal in the DUACS Gridded Product

The DUACS gridded data product uses the same along-track altimetry data that we use here, but it is produced by using a Gauss–Markov (or ''optimal interpolation'') estimate that is intended to take account of prior information about the autocovariance of the measurement noise and the underlying physical signal. The filtering properties of the Gauss–Markov estimate will depend on 1) the assumed SSH and error covariance functions, 2) the assumed signal-to-noise ratio, and 3) the time–space sampling.

The assumed error covariance includes a contribution from uncorrelated random errors and from errors that are correlated along the satellite track to account for so-called long-wavelength orbit and geophysical correction errors (Pujol et al. 2016). This long-wavelength error correction provides a means of identifying and removing signals that are correlated along the satellite tracks but not between different tracks and is an effective strategy (Le Traon et al. 1998) for removing errors in the estimated orbit and errors in atmospheric corrections (e.g., wet tropospheric delay). The LWE correction is especially important for the missions that have less precisely known spacecraft altitudes and orbits (like *ERS-1*). The LWE correction also would tend to remove any real oceanic variability that has large scales along satellite tracks and that is incoherent from one track to another (e.g., because the cross-track length scale or the time scale is shorter than the separation between successive tracks). The DUACS along-track data product that we used to produce the gridded dataset described in appendix A includes the LWE correction (AVISO/CLS 2015), so, while the LWE correction may remove some of the barotropic signal of interest, it does not explain any difference between our gridded product and the DUACS product.

The assumed SSH covariance function involves temporal and spatial decorrelation scales and a propagation speed and direction that vary as a function of latitude and longitude (Pujol et al. 2016). The actual values of the temporal and spatial decorrelation scales used in the DUACS product are not publicly available, but Pujol et al. (2016) show the zonally averaged value of the decorrelation time scale and zonal length scale (their Fig. 4). Between the equator and 20°N, the zonally averaged decorrelation time scale triples (from about 10 days to about 30 days). This assumed decorrelation time scale could have a profound effect on the spatial variations of 30-day variance in the DUACS product.

To investigate this possibility, we performed an analysis identical to the one that led to the plots of 33-day spectral density, squared coherence amplitude, phase, and gain (Figs. 4–7) using the DUACS2014 product. To have an amount of spatial smoothing similar to that in the gridded SSH product that we made, we filtered the DUACS2014 product with a Gaussian weighted average smoother that had half-amplitude wavelengths of 2° in latitude and longitude (meaning that the amplitude of the variability is reduced by 1/2 for wavelengths of 2°, with stronger filtering at shorter wavelengths). We then subsampled the DUACS data product to the 0.5° × 0.5° latitude–longitude grid used for our gridded product and performed exactly the same calculations (with the same code) used to generate Figs. 4–7.

Comparison of the 33-day variance in the DUACS2014 product with that in the gridded SSH product described in appendix A (Fig. 12) shows quantitatively close agreement in some of the major areas of 33-day variance. This is perhaps most obvious in the tropical Pacific, where there is close agreement in both the patterns and the absolute level of 33-day variance; the two estimates are essentially indistinguishable (within 95% confidence intervals) within 10°S–10°N. In this region, the DUACS mapping procedure uses a short correlation time scale in the autocovariance function (Pujol et al. 2016). Despite these quantitative similarities in the tropical Pacific, the global-scale patterns of the 33-day variance maps look completely different, with differences exceeding a factor of 100 in many places and over vast regions (especially in the 20°–40°N region). (A factor of 100 is more than 25 times larger than the 95% confidence interval).

Despite the large difference in the spatial pattern of 33-day variance, the spatial patterns of squared coherence amplitude and phase are quite similar in the DUACS gridded product and the one analyzed here (cf. Fig. B1 with Figs. 5–7). Given that our SSH product was deliberately constructed to have spatially uniform temporal filtering, it seems like spatial variations in the temporal filtering in the DUACS product provide the most

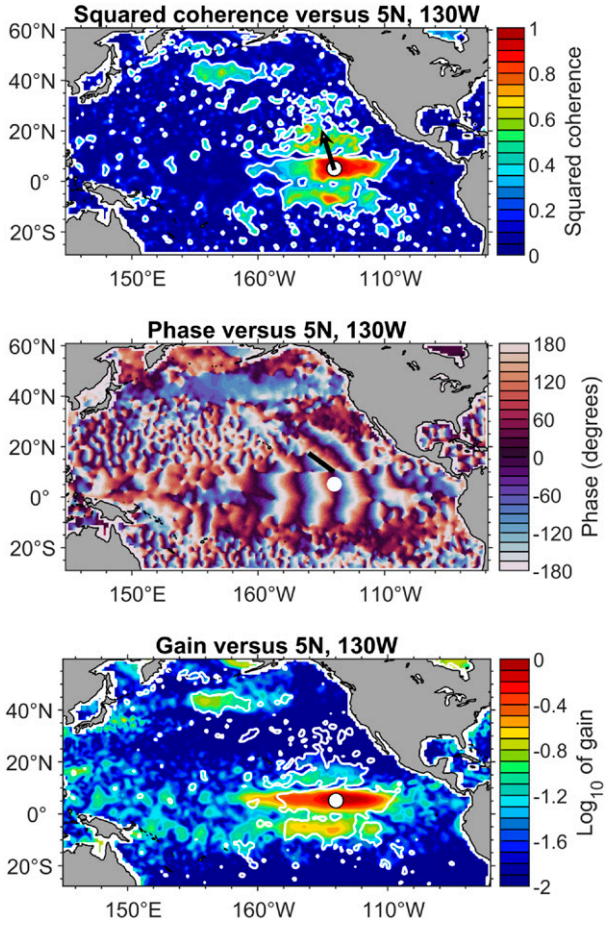

FIG. B1. (top) Squared coherence amplitude, (middle) phase, and (bottom) gain vs 5°N, 130°W in the DUACS2014 gridded SSH product (Pujol et al. 2016). These plots should be compared with Figs. 5–7.

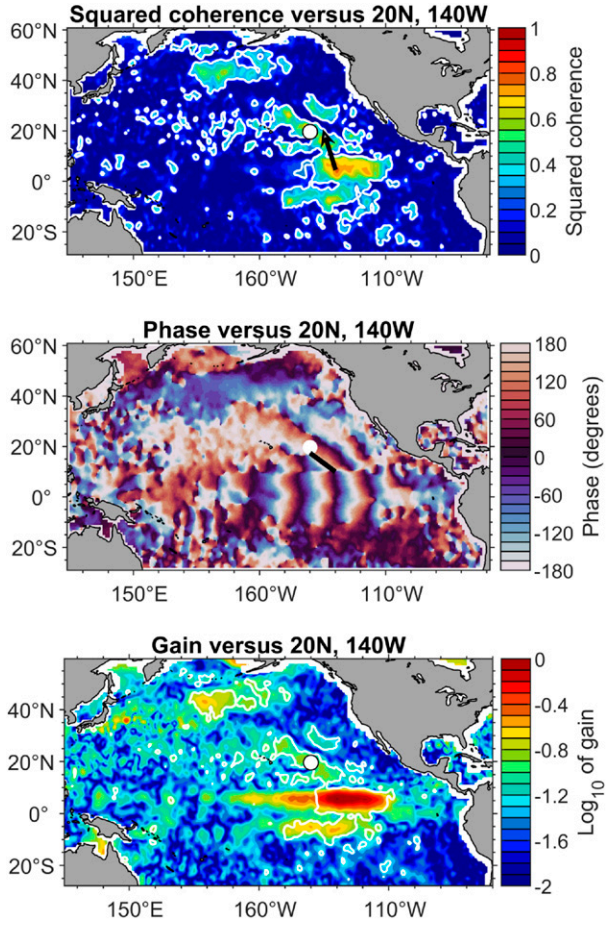

FIG. C1. (top) Squared coherence amplitude, (middle) phase, and (bottom) gain computed using a different reference location (20°N, 140°W, indicated by a white circle in each panel). To aid comparison with Figs. 6 and 7, the gain has been renormalized to equal 1 at 5°N, 130°W, and a uniform offset has been applied to the phase so that it is equal to 0° at 5°N, 130°W. These plots should be compared with Fig. C2 and Figs. 5–7.

obvious way to rationalize the large difference in 33-day variance and the similarity in phase and coherence. This observation is not meant to be a criticism of the DUACS product, because the time scales for the autocovariance function have been carefully optimized for representation of mesoscale eddies. For most purposes, the DUACS product probably provides a better estimate of SSH variability, but it is not appropriate for tracking the propagation of ~30-day waves over thousands of kilometers.

APPENDIX C

Sensitivity to Choice of Reference Location

For the analysis in the main text, the reference location for the cross-spectral calculations was chosen as the place where the TIW SSH signal is strongest (5°N, 130°W, which we will refer to here as the ''primary reference location''). In this appendix, we present representative results obtained using other choices for the reference location.

The gross patterns of squared coherence amplitude, coherence phase, and gain are very similar to those seen in the main text when using reference locations where the SSH signal is coherent with that at the primary reference location. For example, Figs. C1 and C2 show the squared coherence amplitude, coherence phase, and gain maps computed using 20°N, 140°W and 43°N, 175°W as reference locations. To facilitate comparison with Figs. 6 and 7, we rescaled the gain to have a value of one at the primary reference location, and we applied a uniform phase offset so that the phase has a value of 0° at the primary reference location.

These alternate reference locations are places where the SSH signal is coherent with that at the primary reference location (Fig. 5), but it is not a trivial result that the spatial patterns of the cross-spectral quantities should be almost the same regardless of whether the reference location is where the TIW SSH signal is strongest (5°N, 130°W) or at 20°N, 140°W or 43°N, 175°W. For example, the variability at 20°N, 140°W could be incoherent with that at 43°N, 175°W, even if they are both coherent with 5°N, 130°W. The similarity of the patterns that

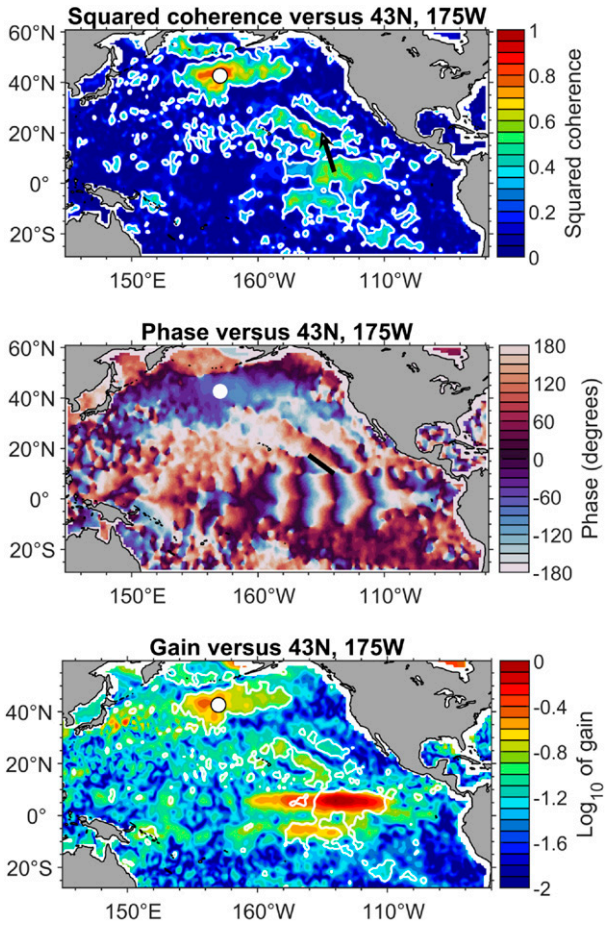

FIG. C2. (top) Squared coherence amplitude, (middle) phase, and (bottom) gain computed using a different reference location (43°N, 175°W, indicated by a white circle in each panel). To aid comparison with Figs. 6 and 7, the gain has been renormalized to equal 1 at 5°N, 130°W, and a uniform offset has been applied to the phase so that it is equal to 0° at 5°N, 130°W. These figures should be compared with Fig. C1 and Figs. 5–7.

result when using different reference locations provides further support to the idea that there is a mutually coherent pattern of variability, which was an underlying assumption of our interpretation of the coherence, gain, and phase patterns.

In fact, the results depicted in Fig. C2 tell us something remarkable: the SSH signal in the northern "hot spot" near 43°N, 175°W is so closely related to the SSH variability in the tropical Pacific that one can use it to explain about half of the SSH variance in the TIW region at 33-day periods and reproduce the pattern of amplitude and phase with surprising detail (cf. lower two panels of Fig. C2 with Figs. 6 and 7).

APPENDIX D

Numerical Model Configuration

The numerical model solves the vertically averaged, linearized, shallow-water equations with variable layer depth:

$$\partial \mathbf{u}/\partial t + f(\theta)\hat{\mathbf{e}}_z \times \mathbf{u} = -g\nabla\eta + h^{-1}\nabla\cdot(hA_h\nabla\mathbf{u}) - R\mathbf{u} \quad \text{and} \tag{D1}$$

$$\partial\eta/\partial t + \nabla\cdot(h\,\mathbf{u}) = 0, \tag{D2}$$

where $\mathbf{u}$ is the horizontal current (with zonal and meridional components u and v), η the SSH displacement, $h(\phi, \theta)$ the variable water depth, f the latitudinally dependent Coriolis parameter, and g the gravitational acceleration. Time is t, and the equations are solved in the spherical-shell coordinates (ϕ, θ) (longitude, latitude), with the local vertical unit vector being $\hat{\mathbf{e}}_z$. The gradients and divergences are strictly horizontal, and a standard Newtonian friction parameterization of the Reynolds stresses is used. Not all of the terms in the stress parameterization are included [see, e.g., Eqs. (13.25) and (13.26) of Müller (2006)], but at the length scales of interest the omitted terms are small relative to the divergence of the momentum gradient.

The finite-difference versions of (D1) and (D2) are solved on an Arakawa C grid with 1° × 1° grid spacing, and the averaging scheme for the Coriolis terms conserves energy globally (e.g., Sadourny 1975). The basin depths are a subsample of ETOPO2 bathymetry. Given the smoothing inherent in producing the gridded SSH product for the coherence calculations, this model gridding should be able to reproduce any features detected in the observations. A limited number of experiments were run using ½° and ⅓° grid spacing. The coastline is set at the 200-m depth, representing the continental shelf break. Small-scale channels and bays with steep bathymetry at high latitudes tend to induce gridscale instabilities that radiate into the rest of the basin, so the North American coastline is smoothed and the Alaskan Peninsula and Aleutian Island chain are modeled as a smoothed, continuous coastline. To ensure that the model feels the full impact of the Emperor Seamount Chain, the ridge line depths from the ETOPO2 one-minute bathymetry are inserted into the ridge-line locations of the one-degree topography. A sponge layer on the western boundary circumvents the necessity of modeling a western boundary, and prevents recirculation of wave energy via spurious coastal Kelvin waves.

Following Warren et al. (2002), the bottom drag is parameterized as friction in an Ekman layer:

$$R = \sqrt{A_v f/2}/h. \tag{D3}$$

We varied the vertical viscosity A_v between 0 and $10^{-2}\,\mathrm{m^2\,s^{-1}}$ [the high end of the range for deep sea viscosities suggested by Johnson (1998)] and found minimal change in the patterns of SSH variability, including little change in the relative amplitudes of recognizable features. The same was true of varying the horizontal viscosity between 1000 and 5000 $\mathrm{m^2\,s^{-1}}$. We display results using $A_h = 2500\,\mathrm{m^2\,s^{-1}}$ and $A_v = 1.6 \times 10^{-3}\,\mathrm{m^2\,s^{-1}}$. These values of viscosity attenuate the gridscale instabilities noted above, and the model reaches an essentially stationary oscillatory state that persists for at least two wave periods before we stop the integration.

REFERENCES

AVISO/CLS, 2015: SSALTO/DUACS User Handbook: (M)SLA and (M)ADT Near-Real Time and Delayed Time Products. AVISO/CLS Tech. Rep., 35 pp., http://www.aviso.altimetry.fr/fileadmin/documents/data/tools/hdbk_duacs.pdf.

Bendat, J. S., and A. G. Piersol, 2010: *Random Data: Analysis and Measurement Procedures*. 4th ed. Wiley-Interscience, 640 pp.

Bloomfield, P., 2000: *Fouerier Analysis of Time Series: An Introduction*. 2nd ed. John Wiley and Sons, 261 pp.

Bower, A. S., and N. G. Hogg, 1992: Evidence for barotropic wave radiation from the Gulf Stream. *J. Phys. Oceanogr.*, **22**, 42–61, https://doi.org/10.1175/1520-0485(1992)022<0042:EFBWRF>2.0.CO;2.

Brink, K. H., and J. Pedlosky, 2020: The structure of baroclinic modes in the presence of baroclinic mean flow. *J. Phys. Oceanogr.*, **50**, 239–253, https://doi.org/10.1175/JPO-D-19-0123.1.

Carrère, L., and F. Lyard, 2003: Modeling the barotropic response of the global ocean to atmospheric wind and pressure forcing-Comparisons with observations. *Geophys. Res. Lett.*, **30**, 1275, https://doi.org/10.1029/2002GL016473.

——, Y. Faugère, and M. Ablain, 2016: Major improvement of altimetry sea level estimations using pressure-derived corrections based on ERA-Interim atmospheric reanalysis. *Ocean Sci.*, **12**, 825–842, https://doi.org/10.5194/os-12-825-2016.

Chelton, D. B., and M. G. Schlax, 1994: The resolution capability of an irregularly sampled dataset: With application to Geosat altimeter data. *J. Atmos. Oceanic Technol.*, **11**, 534–550, https://doi.org/10.1175/1520-0426(1994)011<0534:TRCOAI>2.0.CO;2.

Cox, M. D., 1980: Generation and propagation of 30-day waves in a numerical model of the Pacific. *J. Phys. Oceanogr.*, **10**, 1168–1186, https://doi.org/10.1175/1520-0485(1980)010<1168:GAPODW>2.0.CO;2.

Ducet, N., P. Y. Le Traon, and G. Reverdin, 2000: Global high-resolution mapping of ocean circulation from TOPEX/Poseidon and ERS-1 and -2. *J. Geophys. Res.*, **105**, 19 477–19 498, https://doi.org/10.1029/2000JC900063.

Durland, T. S., and J. T. Farrar, 2020: Another note on Rossby wave energy flux. *J. Phys. Oceanogr.*, **50**, 531–534, https://doi.org/10.1175/JPO-D-19-0237.1.

Egbert, G. D., and S. Y. Erofeeva, 2002: Efficient inverse modeling of barotropic ocean tides. *J. Atmos. Oceanic Technol.*, **19**, 183–204, https://doi.org/10.1175/1520-0426(2002)019<0183:EIMOBO>2.0.CO;2.

Farrar, J. T., 2008: Observations of the dispersion characteristics and meridional sea level structure of equatorial waves in the Pacific Ocean. *J. Phys. Oceanogr.*, **38**, 1669–1689, https://doi.org/10.1175/2007JPO3890.1.

——, 2011: Barotropic Rossby waves radiating from tropical instability waves in the Pacific Ocean. *J. Phys. Oceanogr.*, **41**, 1160–1181, https://doi.org/10.1175/2011JPO4547.1.

Harris, F., 1978: On the use of windows for harmonic analysis with the discrete Fourier transform. *Proc. IEEE*, **66**, 51–83, https://doi.org/10.1109/PROC.1978.10837.

Hogg, N. G., 1988: Stochastic wave radiation by the Gulf Stream. *J. Phys. Oceanogr.*, **18**, 1687–1701, https://doi.org/10.1175/1520-0485(1988)018<1687:SWRBTG>2.0.CO;2.

Holmes, R. M., and L. N. Thomas, 2016: Modulation of tropical instability wave intensity by equatorial Kelvin waves. *J. Phys. Oceanogr.*, **46**, 2623–2643, https://doi.org/10.1175/JPO-D-16-0064.1.

Jayne, S., N. Hogg, and P. Malonotte-Rizzoli, 1996: Recirculation gyres forced by a beta-plane jet. *J. Phys. Oceanogr.*, **26**, 492–504, https://doi.org/10.1175/1520-0485(1996)026<0492:RGFBAB>2.0.CO;2.

Johnson, G. C., 1998: Deep water properties, velocities, and dynamics over ocean trenches. *J. Mar. Res.*, **56**, 329–347, https://doi.org/10.1357/002224098321822339.

Lee, T., J. Farrar, S. Arnault, D. Meyssignac, W. Han, and T. Durland, 2018: Monitoring and interpreting the tropical oceans by satellite altimetry. *Satellite Altimetry Over Ocean and Land Surfaces*, D. Stammer and A. Cazenave, Eds., CRC Press, 231–270.

Le Traon, P. Y., F. Nadal, and N. Ducet, 1998: An improved mapping method of multisatellite altimeter data. *J. Atmos. Oceanic Technol.*, **15**, 522–534, https://doi.org/10.1175/1520-0426(1998)015<0522:AIMMOM>2.0.CO;2.

——, Y. Faugére, F. Hernandez, J. Dorandeu, F. Mertz, and M. Ablain, 2003: Can we merge *GEOSAT Follow-On* with TOPEX/Poseidon and *ERS-2* for an improved description of the ocean circulation? *J. Atmos. Oceanic Technol.*, **20**, 889–895, https://doi.org/10.1175/1520-0426(2003)020<0889:CWMGFW>2.0.CO;2.

Longuet-Higgins, M., 1965: Planetary waves on a rotating sphere. *Proc. Roy. Soc.*, **279A**, 40–68, https://doi.org/10.1098/rspa.1964.0116.

Lyman, J. M., D. B. Chelton, R. A. deSzoeke, and R. M. Samelson, 2005: Tropical instability waves as a resonance between equatorial Rossby waves. *J. Phys. Oceanogr.*, **35**, 232–254, https://doi.org/10.1175/JPO-2668.1.

Miller, A. J., and Coauthors, 2007: Barotropic Rossby wave radiation from a model Gulf Stream. *Geophys. Res. Lett.*, **34**, L23613, https://doi.org/10.1029/2007GL031937.

Mizuta, G., 2009: Rossby wave radiation from an eastward jet and its recirculations. *J. Mar. Res.*, **67**, 185–212, https://doi.org/10.1357/002224009789051227.

Müller, P., 2006: *The Equations of Oceanic Motion*. Cambridge University Press, 291 pp.

Pujol, M.-I., Y. Faugère, G. Taburet, S. Dupuy, C. Pelloquin, M. Ablain, and N. Picot, 2016: DUACS DT2014: The new multi-mission altimeter data set reprocessed over 20 years. *Ocean Sci.*, **12**, 1067–1090, https://doi.org/10.5194/os-12-1067-2016.

Rhines, P., 1970: Edge-, bottom-, and Rossby waves in a rotating stratified fluid. *Geophys. Fluid Dyn.*, **1**, 273–302, https://doi.org/10.1080/03091927009365776.

Sadourny, R., 1975: The dynamics of finite difference models of the shallow-water equations. *J. Atmos. Sci.*, **32**, 680–689, https://doi.org/10.1175/1520-0469(1975)032<0680:TDOFDM>2.0.CO;2.

Schlax, M. G., and D. B. Chelton, 1992: Frequency domain diagnostics for linear smoothers. *J. Amer. Stat. Assoc.*, **87**, 1070–1081, https://doi.org/10.1080/01621459.1992.10476262.

——, ——, and M. H. Freilich, 2001: Sampling errors in wind fields constructed from single and tandem scatterometer datasets. *J. Atmos. Oceanic Technol.*, **18**, 1014–1036, https://doi.org/10.1175/1520-0426(2001)018<1014:SEIWFC>2.0.CO;2.

Smith, R., 1971: The ray paths of topographic Rossby waves. *Deep-Sea Res.*, **18**, 477–483, https://doi.org/10.1016/0011-7471(71)90071-4.

Song, Y. T., and V. Zlotnicki, 2004: Ocean bottom pressure waves predicted in the tropical Pacific. *Geophys. Res. Lett.*, **31**, L05306, https://doi.org/10.1029/2003GL018980.

Spall, M. A., 1992: Rossby wave radiation in the Cape Verde frontal zone. *J. Phys. Oceanogr.*, **22**, 796–807, https://doi.org/10.1175/1520-0485(1992)022<0796:RWRITC>2.0.CO;2.

Thompson, R. O. R. Y., 1979: Coherence significance levels. *J. Atmos. Sci.*, **36**, 2020–2021, https://doi.org/10.1175/1520-0469(1979)036<2020:CSL>2.0.CO;2.

Warren, B. A., T. Whitworth, and J. H. LaCasce, 2002: Forced resonant undulation in the deep Mascarene Basin. *Deep-Sea Res. II*, **49**, 1513–1526, https://doi.org/10.1016/S0967-0645(01)00151-5.

Waterman, S., and S. R. Jayne, 2011: Eddy-mean flow interactions in the along-stream development of a western boundary current jet: An idealized model study. *J. Phys. Oceanogr.*, **41**, 682–707, https://doi.org/10.1175/2010JPO4477.1.

——, N. G. Hogg, and S. R. Jayne, 2011: Eddy–mean flow interaction in the Kuroshio Extension region. *J. Phys. Oceanogr.*, **41**, 1182–1208, https://doi.org/10.1175/2010JPO4564.1.

Weijer, W., 2008: Normal modes of the Mascarene Basin. *Deep-Sea Res. I*, **55**, 128–136, https://doi.org/10.1016/j.dsr.2007.10.005.

——, F. Vivier, S. T. Gille, and H. A. Dijkstra, 2007: Multiple oscillatory modes of the Argentine Basin. Part I: Statistical analysis. *J. Phys. Oceanogr.*, **37**, 2855–2868, https://doi.org/10.1175/2007JPO3527.1.

Wunsch, C., 1989: Sampling characteristics of satellite orbits. *J. Atmos. Oceanic Technol.*, **6**, 891–907, https://doi.org/10.1175/1520-0426(1989)006<0891:SCOSO>2.0.CO;2.